Acta Materialia 303 (2026) 121697

Contents lists available at ScienceDirect

Acta Materialia

journal homepage: www.elsevier.com/locate/actamat

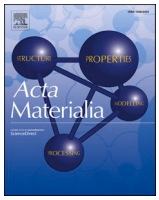

Full length article

Stress-induced amorphization promotes grain boundary sliding in olivine

Ihtasham Ul Haq [a], Patrick Cordier [b,c], Jean Furstoss [b,1], Karine Gouriet [b], Ankush Kashiwar [a,d], Paul Baral [d,2], Andrey Orekhov [a], Nicolas Gauquelin [a], Sanae Koizumi [e], Caroline Bollinger [f], Laurent Delannay [d], Philippe Carrez [b], Thomas Pardoen [d,g], Dominique Schryvers [a], Hosni Idrissi [d,*]

[a] Electron Microscopy for Materials Science (EMAT), University of Antwerp, B-2020 Antwerp, Belgium
[b] Univ. Lille, CNRS, INRAE, ENSCL, UMR 8207 - UMET - Unité Matériaux et Transformations, F-59000 Lille, France
[c] Institut Universitaire de France, 1 rue Descartes, F-75005 Paris, France
[d] Institute of Mechanics, Materials and Civil Engineering, UCLouvain, B-1348 Louvain-la-Neuve, Belgium
[e] Earthquake Research Institute, University of Tokyo, Tokyo, Japan
[f] IRAP, Université de Toulouse, CNRS, CNES, UPS, Toulouse, France
[g] WEL Research Institute, Avenue Pasteur 6, 1300 Wavre, Belgium

ARTICLE INFO

Keywords:
Olivine
Grain boundary sliding, Amorphization
Role of Fe

ABSTRACT

Stress-induced amorphization has recently attracted attention as a potential deformation mechanism in ceramics, semi-conductors or minerals. Its activation is promoted when conventional plasticity, *e.g.* driven by dislocations, is inhibited. However, the mechanisms underlying this phenomenon are still unclear. Based on quantitative *in situ* TEM tensile testing of small-sized olivine bi-crystals, we demonstrate that stress-induced amorphization and grain boundary sliding can be activated under high stresses at room temperature in specimens with high angle grain boundaries. Low angle grain boundaries are less prone to this phenomenon. Varying the iron content in olivine demonstrates that iron inhibits amorphization and, consequently, promotes brittle failure. This contrast with the accepted view that iron promotes ductility but at high temperatures. These findings coming from natural minerals provide a novel approach regarding the control of the mechanical properties of hard materials at low temperatures.

1. Introduction

When crystalline materials are subjected to stress in excess of their yield point, irreversible deformation accumulates as a result of the formation of defects such as dislocations, twins and grain boundaries (GBs), and of their motion. This fundamental state of affairs enables metals forming, opening up a wide range of applications. In ceramics and silicates, conventional plasticity based on dislocation activity is usually inhibited, except at high temperatures. This results in brittleness, as the fracture stress is attained before the yield stress. In the case of ceramics, this represents a significant obstacle to the development of technological applications [1]. In nature, this phenomenon is observed in the cold lithosphere, where rocks exhibit brittle or semi-brittle behavior. This phenomenon is particularly prevalent in fault zones, where plate tectonic movements are localized [2]. Recently, solid-state amorphization has been proposed as an important deformation mechanism in a wide range of materials [3,4] to accommodate deformation and relax the stress, without the need to activate dislocations [5]. This mechanism has been described in particular in olivine [6,7], a silicate which is the most volumetrically abundant mineral in Earth's upper mantle and in the lithospheric mantle. It gives rise to intracrystalline shear lamellae [3,6], and also enhances grain boundary sliding [7,8]. The latter situation is of particular theoretical interest, since, except in the case of nanomaterials, grain boundaries generally have a hardening effect at low temperatures. A better appraisal of the mechanisms occurring naturally in the Earth mantle is not only important in the context of geological studies but can guide the development of novel engineering systems through a type of geo-inspiration.

* Corresponding author.
E-mail address: hosni.idrissi@uclouvain.be (H. Idrissi).
[1] Present address: Departement of Physics and Mechanics of Materials, Institut P', CNRS UPR 3346, Université de Poitiers, SP2MI, F86073 Poitiers, France
[2] Present address: Mines Saint-Etienne, Univ Lyon, CNRS UMR 5307LGF, Centre SMS, 158 Cours Fauriel, 42023 Saint-Etienne, France

https://doi.org/10.1016/j.actamat.2025.121697
Received 13 March 2025; Received in revised form 31 October 2025; Accepted 2 November 2025
Available online 4 November 2025

The present study unravels, for the first time, the mechanisms at the origin of Stress Induced Amorphization (SIA) in olivine using a micro/nanomechanical approach. For this purpose, small olivine bi-crystals with pre-selected single GBs are deformed using quantitative uniaxial tension inside a transmission electron microscope (TEM) using a push-to-pull (PTP) device [9,10], as illustrated in Fig. 1 and described in the Methods section. Specimens for *in situ* deformation are extracted from cross-sectional TEM foils prepared via focused ion beam (FIB) on bulk olivine samples. This method enables the preparation of bi-crystals with grain boundaries pre-selected in terms of their character and of the orientation of the boundary plane relative to the tensile axis (Fig. 1). Some recent studies in the literature reported Ga segregation at grain boundaries during FIB milling of metals with an impact on the mechanical response [11–13]. In the present work, the presence of some residual Ga at GBs cannot be totally excluded. However, the GBs that we studied have shown different behaviors while the PTP specimens were 'FIBed' under identical conditions. This indicates that the presence of Ga (even not confirmed) is not the main player. Table 1 provides a summary of the characteristics of the PTP specimens. It includes the elastic modulus, fracture strain and fracture stress, and the type of GB. We demonstrate that the use of such small specimens allows for the investigation of the limits of ductility and for the attainment of stress levels large enough to initiate mechanical instabilities at the origin of amorphization at GBs, even at room temperature (RT). Olivine is a family of minerals with the chemical formula $(Mg, Fe)_2SiO_4$. The pure magnesium end-member Mg_2SiO_4 is called forsterite. On Earth, the iron content is typically 10 %, whereas on Mars, it is approximately double this value. The role of Fe is investigated by deforming olivine bi-crystals with and without Fe, and the results are consolidated using first-principles calculations. This advanced micro/nanomechanical approach establishes the foundation for the exploration of SIA in a multitude of other materials where it has been documented, but for which the underlying mechanisms remain largely unexplored [3,7,14–20]. In this study, we demonstrate, for the first time, the possibility of extracting the elementary mechanisms driving SIA and the nanomechanical response of GB sliding on specimens including a single GB inside the TEM.

2. Methods

2.1. Specimen preparation

Olivine samples were synthesized from mixed, cold-pressed and sintered powders. SiO_2 and $Mg(OH)_2$ powders were used for forsterite, while SiO_2, MgO and Fe_2O_3 powders were used for ferruginous olivines. In order to follow the mechanical response and the mechanisms of GB sliding, bi-crystal and tri-crystal specimens for push-to-pull (PTP) tensile tests were prepared from pristine bulk specimens (with and without iron) by Focused Ion Beam (FIB). First, cross-sectional foils are prepared by FIB to select grain boundaries with the desired character and orientation relative to the tensile axis (Fig. 1). Special care is taken to avoid the presence of intragranular dislocations in the selected PTP specimens to favor GB sliding. This step is carried out using bright field TEM (BF-TEM) in a Thermo Fisher - Tecnai G2 transmission electron microscope operating at 200 kV and automated crystallographic orientation and mapping in TEM (ACOM-TEM). The foils are then transferred to the PTP device using an Omni-probe micromanipulator in a Thermo Fisher dual beam FIB/SEM (Helios Nanolab 650) and fixed on both sides of the central gap of the PTP (Fig. 1) with e-beam deposited Pt. Finally, a dog bone shaped tensile PTP specimen with selected grain boundaries is obtained by Ga^+ ion beam (30 kV/80 pA) FIB milling. The thickness of the sample is kept around 250 nm.

2.2. Transmission electron microscopy

ACOM-TEM was used to extract the nature of the GBs (rotation axis, misorientation angle and GB plane). This was achieved in a Tecnai G2 TEM operating at 200 kV equipped with the ASTAR system from *Nanomegas*. The electron probe size was ~1.8 nm with a precession angle of 0.5° to minimize dynamical effects. The data were post-treated with the orientation imaging microscopy (OIM) analysis software from EDAX. In the ASTAR system, electron diffraction spot patterns are indexed by comparing individually obtained patterns via cross-correlation matching techniques with pre-calculated electron diffraction templates generated every 0.5° (orientation resolution). All the orientation maps of olivine have been presented in the *Pbnm* space group. EELS was conducted on the QuanTEM, a FEI Titan3 microscope equipped with a Gatan K2 Summit camera placed at the back of a Quantum GIF. For these measurements, the microscope was operated at 300 kV in the monochromated mode, providing an energy resolution of 150 meV. A beam current of 30 pA was selected to limit the beam induced damage and a large collection angle, increasing the EELS signal intensity, was allowed by the use of the EFSTEM camera lengths. An energy dispersion of 0.25 eV/pixel was used with an exposure time of 0.2 s/pixel at 100 % duty cycle of the K2 summit camera as described elsewhere [3].

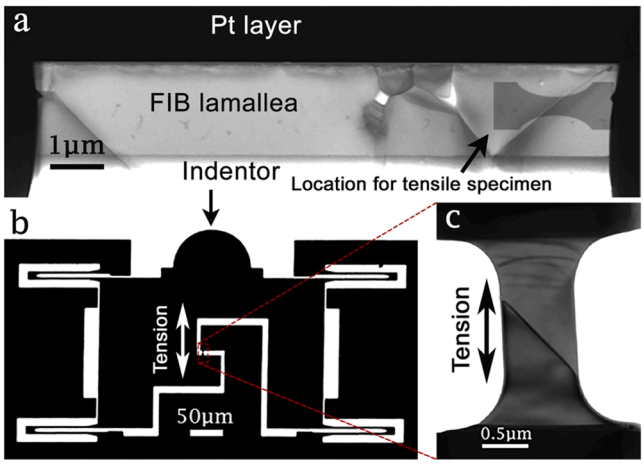

Fig. 1. *In situ* nanomechanical tensile specimen Forsterite-TS-001 preparation. a) BF-TEM image of a cross-sectional FIB foil used for the selection of the GB that will be deformed. b) TEM overview image of PTP chip with olivine bi-crystal specimen located in the center as shown in the magnified BF-TEM image in c). The specimen in (c) was cut by FIB from the area indicated by black arrow in (a).

2.3. In situ TEM nanomechanical testing

The PI 95 TEM Pico Indenter holder with a Push-to-Pull (PTP) device (Bruker. Inc) was used to perform quantitative *in situ* TEM tensile tests. The PI-95 has an integrated diamond flat punch used to apply a compressive force on the semi-circular end of the PTP device (Fig. 1). The load and displacement function of the transducer exhibit a resolution of 3 nN and 0.02 nm, respectively. The force applied on the specimen is obtained by subtracting the contribution of the PTP device from the total applied force. After fracture, the spring constant of the PTP device is measured by performing the *in situ* test without the specimen. The engineering stress is determined by dividing the force on the specimen by the cross-section area inside the SEM/FIB dual beam instruments. This is achieved after cutting one part of the fractured specimen by FIB and by aligning the cross-section area perpendicular to the electron beam. The engineering strain is extracted by dividing the displacement by the initial gauge length. The displacement is measured over frames of the *in situ* movie with digital image correlation (DIC). The *in situ* tensile tests are performed in a Thermo-Fisher Osiris microscope operating at 200 kV under the load control mode.

Table 1
Summarized technical data for all the PTP tensile experiments described in this study.

Specimens	Type	GBS	Type of the GB	Loading rate (μN/*sec*)	Angle with tensile axis	Young's modulus (GPa)	Fracture Stress (GPa)	Fracture Strain (%)
In-situ TEM nanomechanical test on Forsterite (Iron free)								
Forsterite -TS-001	Bi-crystal	Yes	HAGB	0.1	45°	143	2.10	2.67
Forsterite-TS-002	Bi-crystal	Yes	HAGB	0.05	Curved GB	160	1.030	0.97
Forsterite-TS-003	Bi-crystal	Yes	HAGB	0.05	Curved GB	–	1.291	–
Forsterite-TS-004	Tri-crystal	Yes	HAGB	0.1	–	75	1.852	3.02
Forsterite-TS-006	Tri-crystal	Yes	HAGB	0.1	–	160	1.21	1.01
Forsterite-TS-007	Bi-crystal	Yes	HAGB	0.1	30.5°	130	2.93	2.77
Forsterite-TS-008	Bi-crystal	Yes	HAGB	0.05	84.5°	225	1.840	0.94
Forsterite-DIC-009	Bi-crystal	Yes	HAGB	0.1	53.5°	134	1.668	2.10
Forsterite-TS-005	Tri-crystal	No	HAGB	0.1	–	157	1.732	1.2
Forsterite-TS-009	Bi-crystal	No	LAGB	0.1	32.5°	93	1.250	4.2
In-situ TEM nanomechanical tests on olivine (Iron content 25 % and 40 %)								
Olivine-HB9–25–1	Bi-crystal	No	HAGB	0.1	65.5°	135	1.67	1.4
Olivine-HB9–25–2	Bi-crystal	No	HAGB	0.1	36.5°	70	2.413	5.48
Olivine-HB9–25–4	Bi-crystal	No	LAGB	0.1	Curved	173	3.38	1.92
Olivine-HB9–40–1	Bi-crystal	No	HAGB	0.1	43.5°	183	1.77	1.1

2.4. Nanoscale digital image correlation (nano-DIC)

A nano-DIC approach was used for the quantification of the small strain onset of the GBS inside the TEM. For this purpose, fine strain markers were deposited on the bi-crystal tensile specimen. A sputter coating machine (Leica EM ACE600) was used for the deposition of a fine Pt speckle pattern. In the context of the speckle pattern intended for nano-DIC measurements, the objective is not to achieve a continuous deposited film, but rather to deposit individual particles. For optimization of the particle size, several attempts were made using holey carbon support films for TEM as substrate material to reach the required size of the speckle pattern. These films are a cheap and reliable way to test the particle size and their distribution before applying these conditions to the real specimen. After optimization of the deposition parameters, a vacuum of 5 Pa and a current of 60 mA was used to deposit the Pt speckle. A FIB prepared bi-crystal tensile specimen was kept inside the sputter coater machine having the stationary stage setting. A very short deposition time of 3 s was used. Under these conditions, the particles are primarily spherule-shaped and homogeneously distributed over the specimen. The final particle size was ~3–5 nm. HAADF-STEM imaging mode was used for image acquisition during straining with the PTP device to avoid/minimize the contribution of diffraction contrast which might affect the quality of the DIC data. After every 5 min, an image of 2048×2048 (611 nm × 611 nm) pixel resolution was acquired with a dwell time of 7 μsec at a camera length of 165 mm (collection angle about 44.88 mrad). The image resolution was around 0.3 nm/pixel. For data processing, the DIC Ncorr software (open-source MATLAB script) developed by Blaber et al. [21] was used. In this data treatment, a subset window of 20×20 pixels with a step size of one pixel and a strain window of 25 pixels has been used.

2.5. Molecular dynamics simulations

Molecular dynamics simulations are conducted with the Large-scale Atomic/Molecular Massively Parallel Simulator (LAMMPS [22]). To model Mg_2SiO_4 forsterite, we use the rigid-ion parameterization proposed by Pedone et al. [23] which accounts for the long-range Coulombic forces (computed through the particle-particle-mesh method [24] as implemented in LAMMPS) and short-range interactions delineated by a Morse function coupled with a repulsive (r^{-12}) term. This potential has been demonstrated to offer a robust description of numerous properties of forsterite, encompassing bulk, surface, defect properties [25], as well as grain boundaries [26].

Atomic model of the high-angle GB present in specimen Forsterite-TS-001, characterized in Fig. 2, is constructed within a periodic orthogonal cell for which two crystals of given orientations have been stacked together. We thus begin by orienting a first crystalline grain (1) such that $(6\overline{2}7)$ planes are normal to the Z-axis of the simulation cell. This is achieved by determining three directions in the rotated crystal, linear combinations of forsterite crystal lattices, making a Cartesian reference frame within a tolerance of 1° The corresponding volume is then filled by replication of Mg_2SiO_4 crystal motif with care of preserving SiO_4 tetrahedra at surfaces of the grain. Following the same methodology, a second grain is constructed to match the disorientation axis and angle determined experimentally. As built, the two crystals display (X,Y) surfaces of different areas. Therefore, both grains are duplicated before being stacked so that the misfits along X and Y are below 0.02. Optimized system size for grains (1) and (2) corresponds to a surface ~27 nm x 22 nm, with $(6\overline{2}7)$ oriented grain (1) containing 529,200 atoms and grain (2) 327,712 atoms. The near-coincidence site lattice of this GB is found close to Σ270. Practically, atomic models are constructed with the help of the homemade AtomHIC code (freely available at https://github.com/JeanFurstoss/AtomHIC). One may note that AtomHIC code also performs a structural analysis of atomic system to distinguish between crystalline or disordered atomic environments according to the computation of order parameters (interested reader may refer to Furstoss et al. [27]).

As built, all systems (grain (1), grain (2) and GB system) are minimized using conjugate-gradient algorithm with a maximum force criteria of 10^{-10} eV.Å^{-1} to compute their respective energies E_1, E_2 and E_{tot}. Because of periodic boundary conditions, the GB system contains two complexions of the investigated GB. Therefore, we estimate the GB mean energy $\overline{\gamma}$ as:

$$\overline{\gamma} = \frac{E_{tot} - E_1 - E_2}{2A}$$

where A taken as 27×22 nm^2, represents the GB boundary area.

Molecular Dynamic simulations of GB shear deformation are performed in the NVT ensemble using a timestep of 1 fs. Shear γ_{xy} is continuously increased every 5 fs, leading to a 2.10^{10} s^{-1} constant shear strain rate.

2.6. First-principles calculations

First-principles calculations for forsterite (Mg_2SiO_4) and fayalite (Fe_2SiO_4) compositions are carried out using VASP calculations [28]. All simulations are static, involving no characteristic timescale. They are based on the density functional theory (DFT) using a plane wave basis set and the projector augmented wave method (PAW) [29]. Exchange–correlation energy is accounted by employing the Perdew-Wang, gradient-corrected functional (GGA) [30]. For fayalite, we rely on

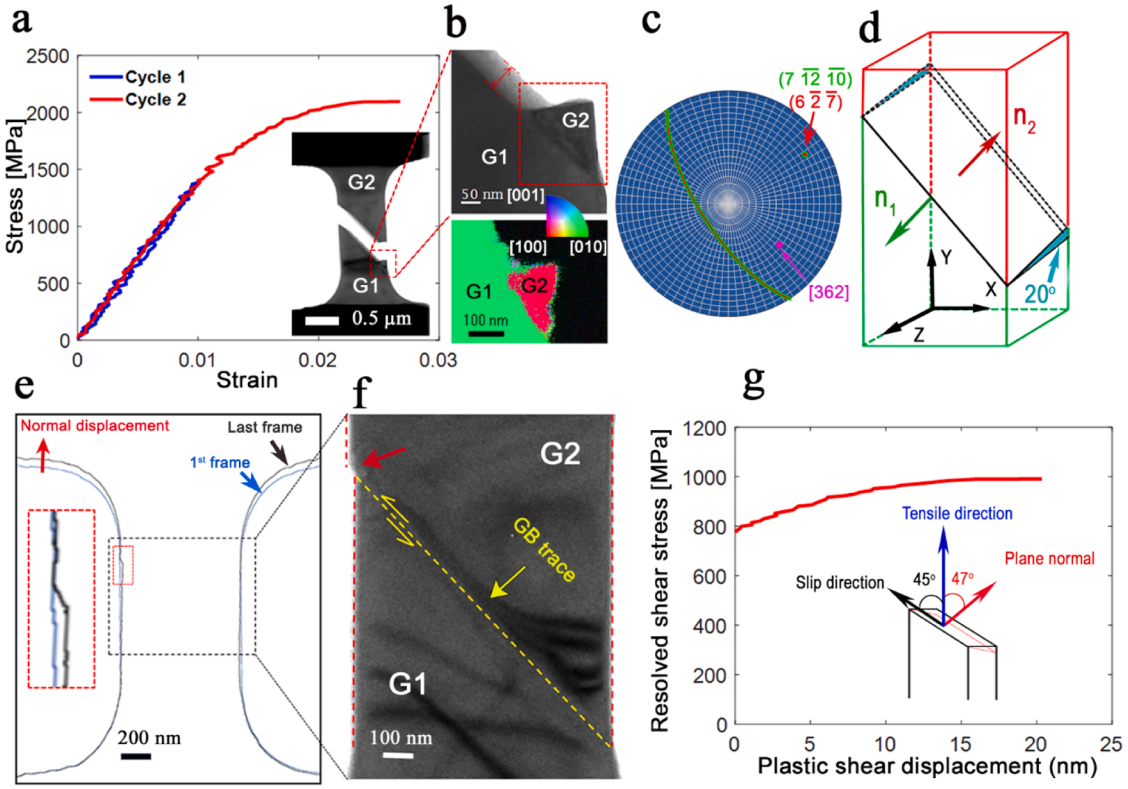

Fig. 2. PTP test on single olivine GB. a) Engineering stress-strain curve on specimen forsterite-TS-001 (Table 1) with BF-TEM image after fracture shown in the inset. b) Magnified image showing a small portion of grain G2 which is still in contact with grain G1 as well as ACOM-TEM analysis of the same area. c,d) Stereographic projection and schematic illustration showing the GB misorientation axis and GB planes in the reference systems of G1 and G2 and the inclination of the GB plane with respect to the surface (~20°), respectively. e) superposition of the first and last frame (just before fracture) of the *in situ* movie. g) GB resolved shear stress (GBRSS) as function of the plastic shear displacement.

GGA+*U*, whereby strong correlation is captured via an additional local Hubbard repulsion of magnitude U [31]. To ensure an adequately atomic force convergence, plane-wave basis set expansion was limited using a kinetic energy cut-off of 520 eV for forsterite and 800 eV for fayalite, coupling here to simplified GGA+*U* = 2.0 eV scheme [31–33].

Glass excess energies, here taken as the excess energy of an amorphous state with respect to the crystalline counterpart, are evaluated for a single atomic amorphous configurations corresponding to either Mg_2SiO_4 or Fe_2SiO_4 chemical composition. The glass structure is obtained from classical MD simulations (as presented above) considering a Mg_2SiO_4 liquid of 228 atoms heated to 3300 K and then quenched using a molecular static scheme. The as-quenched configurations are then minimized using VASP to compute the glass configuration energy and volume corresponding to the respective chemical composition Mg_2SiO_4 and Fe_2SiO_4.

First-principles calculations have also been used to investigate the brittle failure of Mg_2SiO_4 and Fe_2SiO_4 compounds by calculating the critical stress for cleavage along the (100), (010) and (001) planes. In such calculations, deformation is localized in the vicinity of a cleavage plane in order to extract the decohesion force of the plane. The initiation of a crack tip can indeed be modelled by two nearly parallel surfaces. The cleavage stress in mode I are thus calculated within a periodic system composed of four unit-cells stacked along the direction of loading. Ideal brittle cleavage is then modelled by incrementally introducing a rigid separation between the two half blocks of the system [34]. As already reported [34], decohesion energy plotted *versus* separation distance shows an initial "elastic" behaviour followed by a region of instability before reaching a constant energy plateau commonly reported as the cleavage energy. In this work, we define the cleavage stress as the stress derived from the so-called Universal Binding Energy Relation [35].

3. Results

3.1. Stress-induced amorphization and GB sliding in Mg_2SiO_4

Fig. 2a shows two loading cycles performed on a Mg_2SiO_4 forsterite bi-crystal. The maximum load was 150 µN for the first deformation cycle (cycle1-blue curve in Fig. 2a). After this cycle, the experiment was stopped in order to set the parameters of the second cycle with a maximum load of 300 µN (cycle2-red curve in Fig. 2a). In this cycle, fracture occurred along the GB (inset in Fig. 2a) at an applied stress of 2.1 GPa and a total strain of 0.026. The strain produced in the linear regime in cycle 1 was fully recoverable. However, plastic deformation occurs in cycle 2 as evidenced by a deviation from the pure elastic regime detected at ~1.5 GPa engineering stress. In Fig. 2e, the superposition of the first and last frame (just before fracture) of the *in situ* movie reveals the presence of a small step at the left edge of the specimen suggesting a displacement along the GB (see also Video S1). No intragranular deformation mechanisms (*e.g.* dislocations) were observed before and during loading. The plastic strain measured in cycle 2 is thus mainly accommodated by GB sliding as shown in Fig. 2e and 2f. No GB sliding was observed at the right edge of the specimen and a small portion of grain G2 is still in contact with grain G1 after fracture in Fig. 2b. This suggests that the sliding process is heterogenous.

The nature of the boundary was characterized after fracture. Fig. 2b shows the analysis of the GB using automated crystallographic orientation mapping in the TEM (ACOM-TEM) on the small portion of the GB which had resisted to GB sliding at the right edge of the specimen. This boundary is a high-angle GB with misorientation angle 85.5° and misorientation axis [362]. The GB plane was identified as $(7\ \overline{12}\ \overline{10})$ (resp. $(6\ \overline{2}\ \overline{7})$) in the reference system of grain G1 (resp. grain G2), see Fig. 2c.

Fig. 2*g* reports the mechanical behavior of a single GB undergoing sliding in terms of the variation of the resolved shear stress as a function the plastic shear displacement. The GB plane is determined by using the Euler angles from ACOM-TEM and the inclination of the GB plane with respect to the surface (~20° in Fig. 2d). This inclination was extracted by measuring the thickness of the specimen (~ 213 nm) and the width of the projection of the GB plane after fracture (red arrows in Fig. 2b). The GB resolved shear stress is calculated as equal to $\sigma\cos(\alpha)\cos(\beta)$, with σ the applied engineering stress, α the angle between the tensile axis and the direction of sliding while β is the angle between the tensile axis and the normal to the GB plane. For the specimen forsterite-TS-001 shown in Fig. 2, $\alpha = 45°$ and $\beta = 48°$. The plastic shear displacement in Fig. 2*g* is determined by measuring the projection of the normal displacement along the direction of sliding. Fig. 2*g* shows that GB sliding occurs under a resolved shear stress of about 800 MPa.

in situ TEM nanomechanical testing was combined with nanoscale digital image correlation (nano-DIC) to further characterize GB sliding (see more details in the Methods section). In Fig. 3a and Fig. 3b, a speckle of Pt nano-particles with an average size of 3–5 nm was sputtered on the olivine bi-crystal. In this case, the boundary is a high-angle GB with a misorientation angle 62.5° and misorientation axis [12 2 1]. The GB plane was identified as ($\bar{2}$ 5 $\bar{5}$) (resp. (4 12 $\overline{11}$)) in the reference system of grain G1 (resp. Grain G2), see Supplementary Fig. S1. The PTP tensile test was performed in the load control mode with a loading rate of 0.1 μN/s. An apparent Young's modulus of 134 GPa was extracted. The stress-strain curve shown in Fig. 3c was extracted by tracking Pt particles in the area indicated by the yellow square in Fig. 3a. Fig. 3c shows that the specimen deforms plastically before breaking along the grain boundary at a tensile stress of about 1.7 GPa and a total strain of 0.021. Careful examination of the edges of the fracture at the GB (Fig. 3d) confirmed the activation of GB sliding similar to the results shown in Fig. 2. Fig. 3e shows the evolution of the displacements along and perpendicular to the GB determined by tracking the Pt particles over the area indicated by the yellow square in Fig. 3a. At about 0.017 macroscopic strain, the displacement field inside the GB region shows a transition from an elastic and homogenous deformation to a second regime where the strain is mainly accommodated by sliding along the GB. Fig. 3f shows the shear strain map obtained from the yellow square in Fig. 3a. Note the heterogeneity of the magnitude of the local shear strain along the GB with values ranging from 1.75 % in the bottom right side to 0.9 % in the upper left side. This is in agreement with the heterogenous sliding of the GB already observed in Fig. 2.

Fig. 4 illustrates detailed characterization by high resolution TEM (HRTEM) of the fracture surface at the GB of Fig. 2. Fig. 4a shows that, amorphization occurred at the GB as demonstrated by the Fast Fourier Transform (FFT-a(2)) in the same figure. Furthermore, small olivine nano-crystallites with different crystallographic orientations are detected within the amorphous phase (FFT-a(3)). Fig. 4b shows another location on the same GB. It shows that some nano-crystallites form twin-like interfaces. These indications point to deformation under high stress.

Molecular dynamics (MD) simulations were conducted to investigate GB sliding in forsterite. We have chosen to carry out a calculation that reproduces the situation of the experiment described in Fig. 2. As described in the Methods section, we build a system containing a GB with a 85° misorientation where the grains coexist along (6$\overline{27}$) and (7 $\overline{12}$ $\overline{10}$) planes. The structure of the as-built GB appears essentially crystalline (Fig. 5a) and the GB energy is $\bar{\gamma} = 1.70\ J.m^{-2}$, a value which compares well with the various GB energies computed previously in forsterite [26,27,36]. The cell is deformed by simple shear at 300 K and 2.10^{10} s^{-1}. The stress-strain curves are shown on Fig. 5c. The elastic regime ends at a peak stress of 3.5 GPa, followed by a weakening of approximately 0.75 GPa leading to a steady state flow at 2.75 GPa. This stress level is higher than that observed experimentally due to a higher strain rate (10^{-5} to 10^{-6} s^{-1} in the PTP tests), the same applies to the elastic domain preceding the amorphization threshold. A similar behavior has already been observed between the experimental [37] and numerical [38] deformations of amorphous olivine alone. During shear, the width of the disordered regions around interfaces increases highlighting that GBs, which localize deformation, undergo amorphization (Fig. 5b). The evolution of the thickness of the amorphous layers with finite shear strain presented in Fig. 5c shows a monotonous increase with strain. This establishes a direct link between the growth of the amorphous layer and plastic shear. In fact, no other intracrystalline deformation mechanism (dislocations) is detected in the crystalline layers. The growth rate of the amorphous layer has an average of 8 Å / 100 % strain. This rate is likely to depend on the GB orientation and misorientation. Further calculations to investigate the role of crystal orientations on SIA are underway and will be presented at a later date.

3.2. *Effect of Fe on SIA and GBS*

Fig. 6 shows the results of PTP tests performed on $(Mg,Fe)_2SiO_4$ olivine bi-crystals with 25 % and 40 % Fe. The boundary in specimen containing 25 % Fe (Fig. 6a) is a high-angle GB with a misorientation angle 55° and a misorientation axis (12 $\bar{3}$ 7), see Supplementary Fig. S2. The GB plane was identified as (1 $\bar{6}$ 1) (resp. (7 7 $\bar{9}$)) in the reference system of grain G1 (resp. Grain G2). This specimen fractured along the GB (Fig. 6d) at an applied stress of 1.67 GPa and a total strain of 0.014 (Fig. 6b) but without any clear evidence of plasticity, in contrast with the Mg_2SiO_4 specimens shown in Fig. 2. There is a slight change of slope from the elastic linear regime (green line in Fig. 6b) around 0.007 strain in the stress-strain curve of Fig. 6b, but no clear evidence of GB sliding can be detected at the magnification of Fig. 6c. Furthermore, there was no evidence of intragranular dislocation activity. Interestingly, Fig. 6d shows the presence of a very thin amorphous layer (~10 nm) at the edge of the cracked boundary. This could explain the slight deviation from elasticity observed in Fig. 6b It is worth noting that, Electron energy loss spectroscopy (EELS) results revealed local enrichment of Fe^{3+} in the amorphous layer (Supplementary Fig. S3) in agreement with Kranjc et al. [6]. However, in contrast with the HRTEM observations of the Mg_2SiO_4 specimen shown in Fig. 4, the thin amorphous layer in Fig. 6e does not exhibit any traces of nanocrystallites. The GB of specimen containing 40 % Fe is a high-angle GB with a misorientation angle 95° and misorientation axis [10 7 $\overline{10}$] (see Supplementary Fig. S4). The GB plane was identified as ($\bar{2}$ $\overline{12}$ 1) (resp. ($\overline{12}$ 3 $\bar{4}$) in the reference system of grain G1 (resp. Grain G2). Fracture occurred along the GB (Fig. 6i) at an applied stress of 1.77 GPa and a total strain of 0.011 but without any evidence of GB sliding (Fig. 6h). In this instance, no amorphous layer could be detected along the cracked GB (Fig. 6j). This finding is consistent with the absence of any indication of plasticity in Fig. 6*g* where there is no clear evidence of deviation from pure elasticity. The Fe content in olivine appears as a crucial factor in the potential activation of GBS and SIA in olivine.

4. Discussion

Stress-induced amorphization promoting GBS was reported in bulk synthetic forsterite aggregates deformed with a Paterson press or triaxial multi-anvil press at temperatures around 1000 °C [7]. This is usually considered as a low temperature regime in this refractory silicate (T_m = 1890 °C) and confining pressure is generally necessary to achieve a ductile regime [39]. Here we show that SIA can be activated at room temperature in the case of very small specimens. This finding agrees with the observations of Kranjc et al. [6]. However, in their case, SIA appeared as shear lamellae in single crystals whereas our study highlights the role of grain boundaries along which SIA is localized. In both cases, the RT activation of SIA is related to the lack of dislocation activity as well as the high stress levels reached in these micromechanical testing experiments. The slightly lower stress levels in our study, compared to those of Kranjc et al. [6], suggest an easier activation of SIA at the

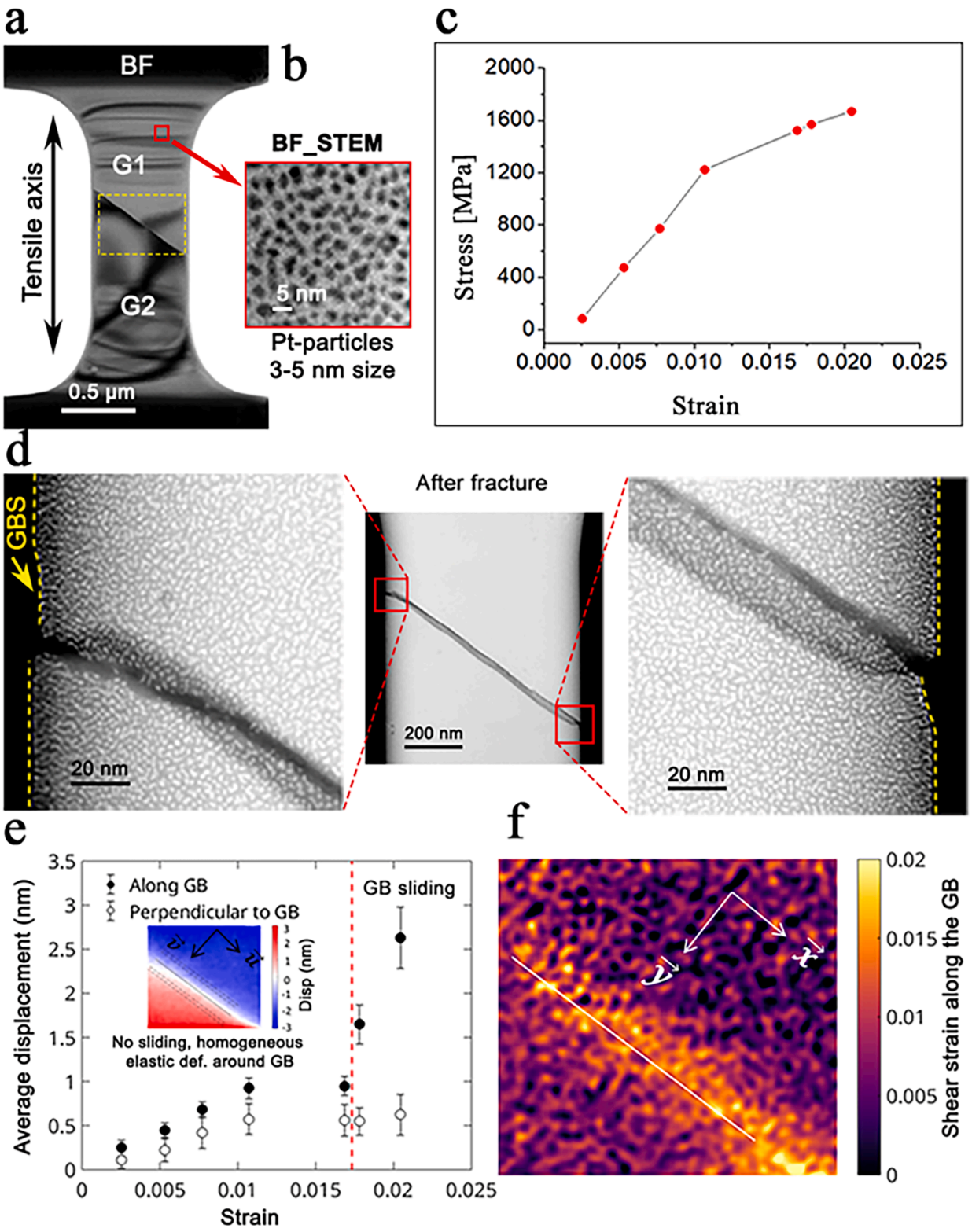

Fig. 3. Nanoscale Digital image correlation. a) BF-TEM image on PTP specimen Forsterite-DIC-009 before deformation. b) magnified image showing the speckle of Pt nano-particles used for nano-DIC. c) stress-strain curve extracted by tracking Pt particles in the area indicated by the yellow square in Fig. 3a. A plastic strain 0.6 % corresponds to 3 nm elongation (since the gauge length is 474 nm). e) Evolution of the displacements along and perpendicular to the GB with strain extracted by tracking the Pt particles over the area indicated by the yellow square in Fig. 3a. Given the orientation of the GB, these displacements correspond to an elongation of 2.1 nm of the sample. f) shear strain map obtained from the yellow square in (a). Note the heterogeneity of the magnitude of the local shear strain along the GB.

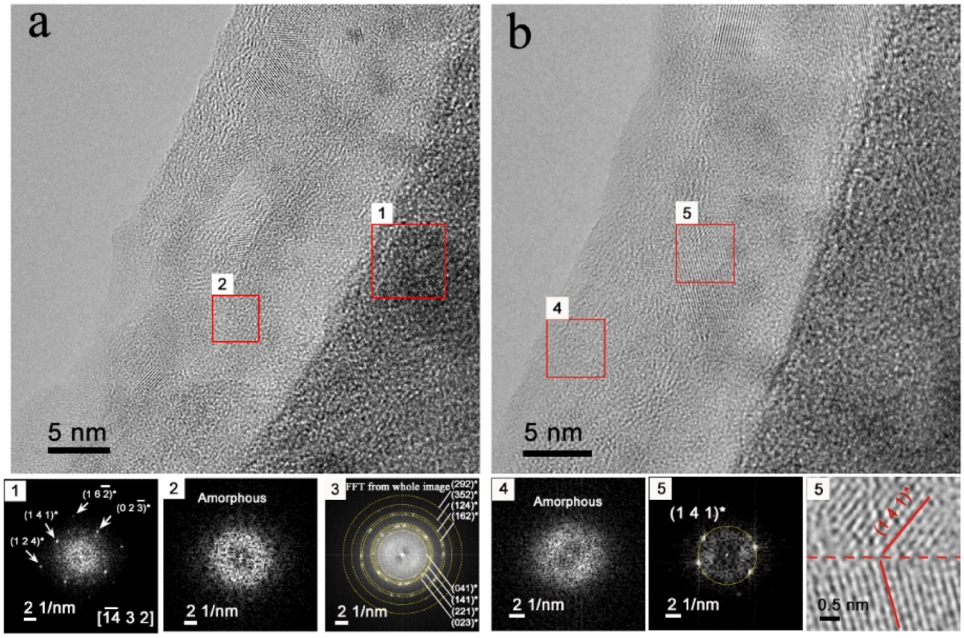

Fig. 4. High resolution TEM analysis after fracture. (a) and (b) HR-TEM images acquired in two different locations on the fracture surface at the GB of Fig. 2 (Forsterite-TS-001 in Table 1). FFTs have been generated from the corresponding red squares shown in the images. Note the formation of amorphous phase in FFT-a (2) and FFT-b(4). FFT-a(1) was generated from the crystal in square (1) while FFT-a(3) was obtained from image (a). The amorphous phase confines small olivine nano-crystallites with different crystallographic orientations as shown in FFT-a (3). Some of these nano-crystallites form twin-like interfaces, see FFT-b(5) and image (5).

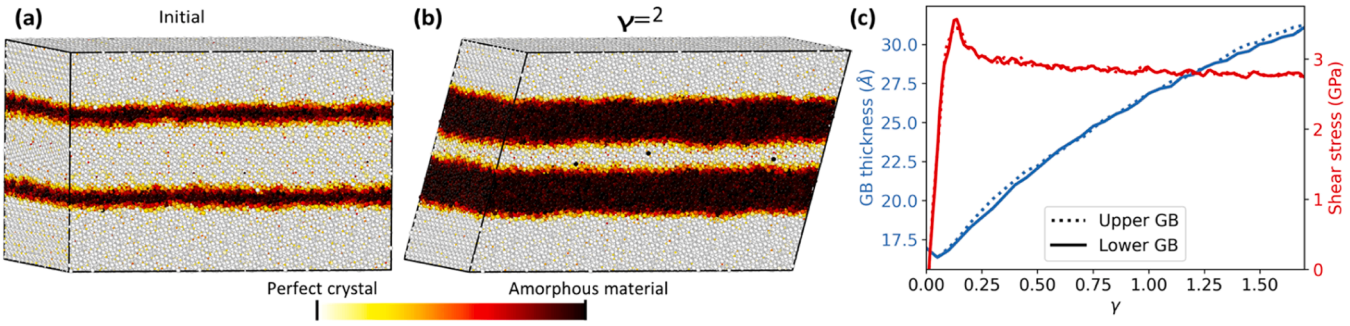

Fig. 5. MD simulations of shear induced amorphization and GB sliding. The simulations were achieved on a GB similar to the Forsterite-TS-001 specimen deformed by the PTP (see Table 1 and Fig. 2). (a) and (b) structure of the GB before and after shear deformation showing GB amorphization. (c) The stress-strain curve together with the evolution of the thickness of the amorphous layer with shear strain. The later shows a monotonous increase of the thickness with strain.

structural defects formed by GBs. Indeed, the experiment in which a specimen containing a LAGB (Forsterite-TS-009, see Table 1 and Supplementary Fig. S5) was deformed did not lead to SIA. However, this conclusion must be taken with caution due to the limited number of LAGBs characterized in the course of the study when compared to HAGBs. More PTP tests on LAGBs will be needed to confirm this trend. The activation of SIA is also probably due to the impossibility of activating non-diffusive plastic deformation mechanisms in olivine GBs. To date, neither electron microscopic characterizations nor numerical modelling [26,27] have demonstrated evidence of glide of dislocations or disconnections in olivine GBs. To confirm this, we carried out dedicated MD simulations (Fig. 5) on a GB similar to the one used in the PTP test (Fig. 2). Apart from SIA, no plasticity mechanism is activated in the GB. GB sliding results from SIA and plastic shear within the amorphous phase at the GB. The thickness of the amorphous phase increases with increasing shear strain demonstrating that SIA is a deformation-producing mechanism. In our experiments, the fracture stress ranges from 1 GPa to 3 GPa while the fracture strain at the GB does not exceed 0.03. This fairly low ductility is due to the small thickness of the specimens which drastically reduces the amplitude of out-of-plane GB sliding. Indeed, amorphous olivine has been shown to exhibit significant ductility at small scales [37].

The use of very small specimens has enabled us to characterize the mechanical behavior of individual GBs. Plastic flow associated with GB sliding was observed at RSS around 800 MPa (Fig. 2*g*). However, despite the very small size of the specimens, it is likely that this value masks significant variation, as the local stress required to activate SIA at a potency site being certainly large. This is suggested by the nano-DIC deformation analysis, which shows inhomogeneous shear strain (Fig. 3), and by the incomplete fracture of the GB of the specimen of Fig. 2b On an even smaller scale, the presence of nano-crystallites within the amorphous phase shown by HRTEM analysis of the fractured GB (Fig. 4) adds to this picture of an heterogenous process. Some of these particles meet and form low energy interfaces such as twin like interfaces. Similar nano-crystallites have been observed in amorphous GBs in bulk olivine deformed with a Paterson press at 0.3 GPa and 950 °C (see Supplementary Fig. S6) and presenting GBS and SIA [7]. This indicates that the same mechanism is activated at RT in the PTP

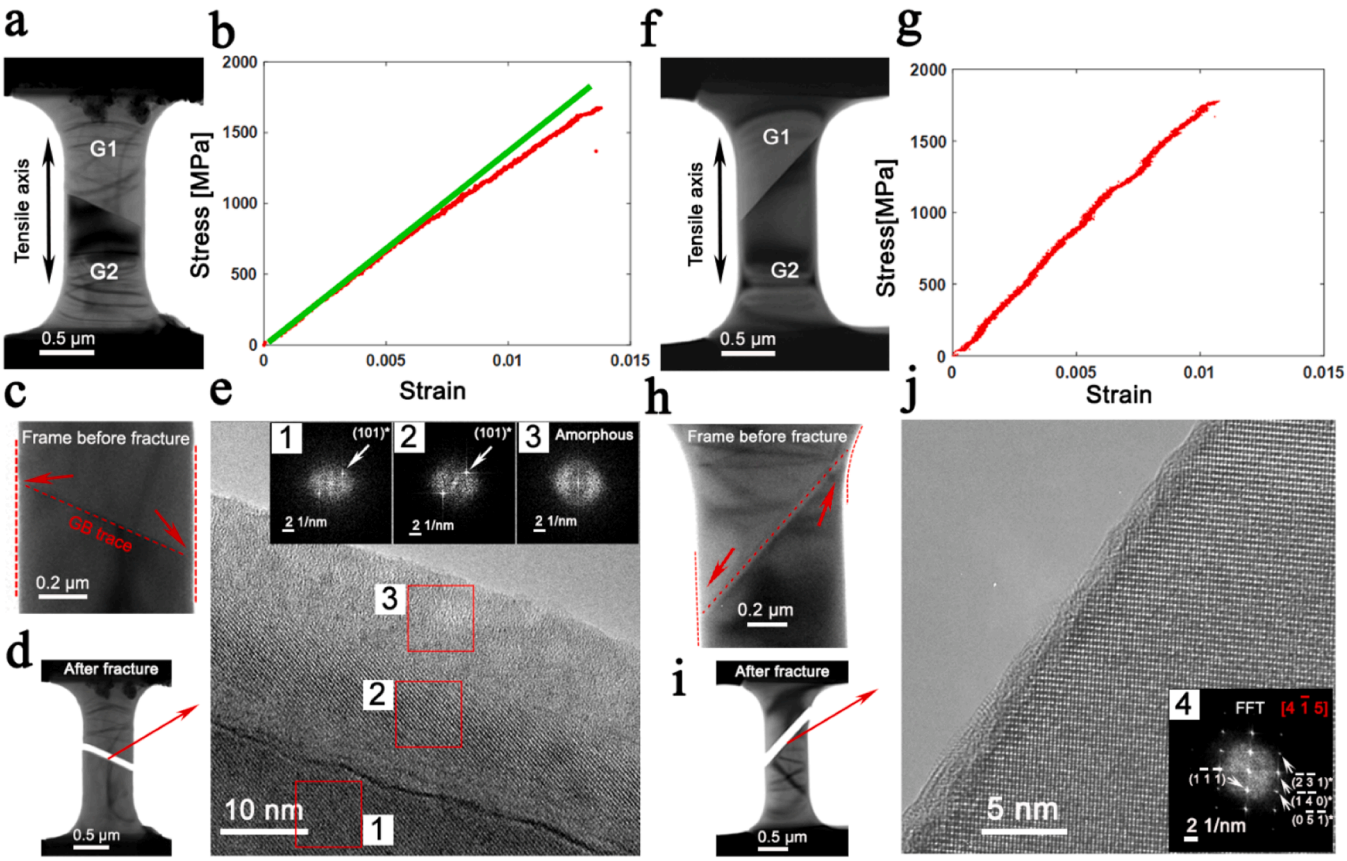

Fig. 6. Effect of Fe on SIA and GBS. Results of PTP tests performed on $(Mg,Fe)_2SiO_4$ bi-crystals with 25 % (specimen Olivine-HB9–25–1 in (a-e)) and 40 % Fe (specimen Olivine-HB9–40–1 (f-j)), respectively. GB sliding is not observed at the magnification of the images in (c) and (h). However, slight deviation from the linear elastic regime can be observed in (b) together with the observation of a tiny amorphous layer at the surface of the fractured GB in (e); see also the FFTs in (e). Such features cannot be detected in (g) and (j).

experiments. We can hypothesize that these amorphization heterogeneities are linked to local structural heterogeneities of the GB (complexions) which, in these silicates with their complex crystallochemistry, can be much more diverse than in metals [40–42]. Further post-mortem and in-situ TEM analysis of GBs have shown shear at the interface together with the crystal-to-amorphous transition at the GB in PTP and bulk olivine specimens deformed with a Paterson press at 0.3 GPa and 950 °C (Supplementary Fig. S7 and Fig. S8) as well as slow and progressive growth of the amorphous layer front at the GB in PTP specimens (Supplementary Fig. S9), which confirm that the amorphous layer at the GB is not an artifact originating from FIB preparation.

The observation that iron-rich samples are more brittle and pure magnesium end-member samples more ductile (albeit with an unusual mechanism involving amorphization) is counter-intuitive given that creep response at high temperatures would impose an opposite view (higher iron content increases ductility, *e.g.* Zhao et al. [43]). To gain a better understanding of this behavior, modelling at atomic scale was performed to compare, in the absence of other plasticity mechanisms, the respective tendencies of olivine to amorphization and brittle fracture. In order to discriminate between the two end-members of olivine, Mg_2SiO_4 forsterite and Fe_2SiO_4 fayalite, with enough degree of accuracy, calculations based on the density functional theory (DFT) are needed since reliable classical MD potentials are not available for Fe ternary compounds. Our understanding of amorphization mechanisms is not sufficiently advanced to allow convincing modeling. Faced with this difficulty, Hu et al. [44] presented a theoretical analysis of the amorphization tendency based on the energy difference between the crystalline and amorphous phases. Excess energy of amorphous Mg_2SiO_4 (Fo) and Fe_2SiO_4 (Fa) computed for the same inherent glass structure leads to $\Delta E_{Fo} = 0.2\ eV/at$ while $\Delta E_{Fa} = 0.23\ eV/at$, suggesting that the amorphous state of fayalite is slightly more energetic than that of amorphous forsterite. However, this difference remains very small and not very decisive compared with those presented in the study by Hu et al. (2023). To further assess the tendency of olivine to amorphize or undergo brittle fracture, we compare the decohesion energy for different planes in these two compounds forsterite and fayalite (Fig. 7). The decohesion energy can be modelled using the following expression, where l_b is a critical length and G_b^{ideal} is the ideal cleavage energy.

$$\Delta E^{ideal} = G_b^{ideal}\left[1 - \left(1 + \frac{x}{l_b}\right)\exp\left(-x/l_b\right)\right]$$

The cleavage energy G_b^{ideal} is a characteristic of a crystallographic plane. Regardless of phase composition, the lowest brittle cleavage energy is found for the (010) plane, while the highest value is found for the (100) plane. However, ideal cleavage energies are systematically found higher in Mg_2SiO_4 forsterite. In terms of cleavage stress, the previous expression can be used to derive the corresponding critical cleavage stress $\sigma_c = G_b^{ideal}/el_b$. As shown in Table 2, the critical cleavage stresses for forsterite are higher than those calculated for fayalite. While chemical composition appears to have a significant effect on mechanical response (amorphization or cleavage) to high stress, it is difficult to see this as a consequence of olivine's intrinsic properties. As our study is based on grain boundary behavior, this difference in behavior suggests an important influence of chemistry on grain boundary structure (complexions) and properties.

SIA-induced GB sliding must be considered in the broader context of olivine deformation. The deformation of olivine has long been discussed [45] in terms of dislocation creep *versus* diffusional creep (Fig. 8).

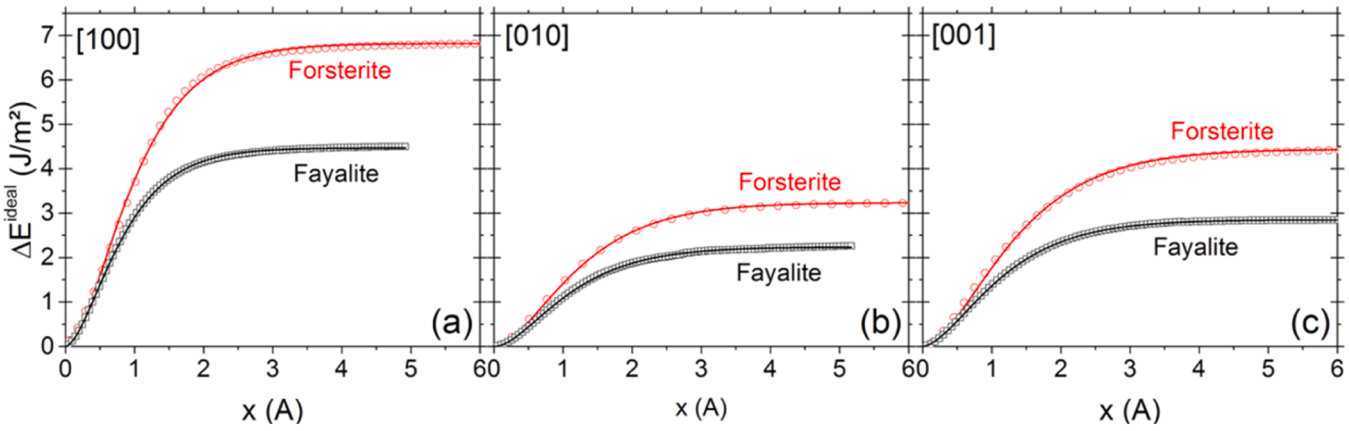

Fig. 7. Decohesive energy ΔE^{ideal} as a function of the rigid opening x of the structure, calculated by DFT for ideal cleavage simulations for forsterite (red) and fayalite (black). (a) cleavage plane (100), (b) cleavage plane (010) and (c) cleavage plane (001). For fayalite, the cleavage threshold is reached for lower cleavage energy, but also at significantly lower cleavage stresses (accordingly to the Universal Binding Energy Relation fitted on the DFT results).

Table 2
Cleavage energy G_b^{ideal}, critical length l_b, and critical cleavage stress σ_c for Fe_2SiO_4 and Mg_2SiO_4.

		G_b^{ideal} (J/m^2)	l_b (Å)	σ_c (GPa)
Forsterite Mg_2SiO_4	(100)	6.83	0.58	43.6
	(010)	3.23	0.67	17.7
	(001)	4.44	0.73	22.4
Fayalite Fe_2SiO_4	(100)	4.48	0.49	33.5
	(010)	2.19	0.57	14.1
	(001)	2.82	0.63	16.5

Although this is not always emphasized, GB sliding significantly contributes to macroscopic strain during diffusional creep [46,47]. In this case it is referred as diffusion-accommodated GB sliding [48]. Additionally, an experimentally identified creep mechanism called DisGBS (for dislocation-accommodated GB sliding) was found to be grain size sensitive on the basis of rheological data on olivine aggregates deformed near the transition between dislocation creep and diffusion creep [49]. Activation of this mechanism was reported in naturally deformed peridotites from upper mantle shear zones [50]. The consideration of DisGBS has expanded the range of conditions under which GB sliding activates, which is typically $T > 1100$ °C, grain sizes <10 μm, $\sigma < 200$ MPa (Fig. 8). Although the contribution of different types of defect activation has been suggested, such as disclinations [51] and disconnections [52], the microscopic mechanisms underlying DisGB sliding are not yet clearly established. It should be noted that the presence of fluids or melts at grain boundaries enhances GB sliding [53]. However, the presence of amorphous films at grain boundaries in these samples after deformation should not be confused with that obtained by solid-state amorphization as described in our study. SIA-induced GB sliding differs significantly from other modes of GB sliding in terms of its activation conditions ($T < 1100$ °C, $\sigma > 1$ GPa). Therefore, it is interesting to highlight a new low-temperature, high-stress domain where SIA-induced GB sliding occurs on deformation maps at the interface between low-temperature plasticity and cleavage fracture (Fig. 8).

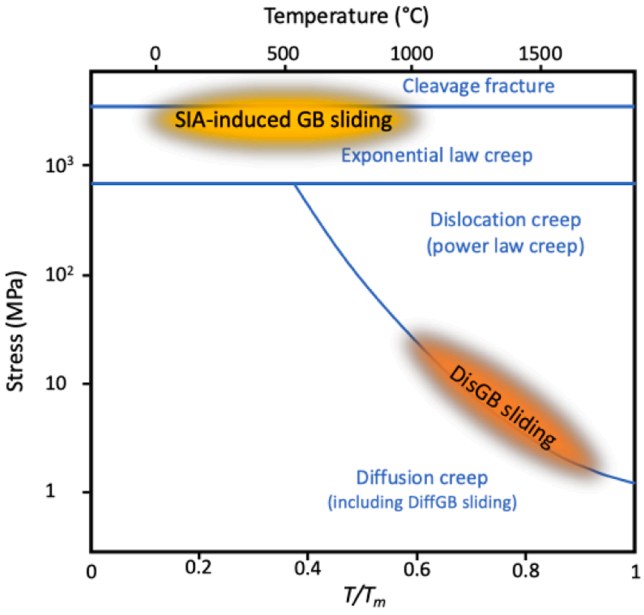

Fig. 8. This deformation map of olivine, taken from [45], shows the various domains in which GB sliding is expected. The area of DisGB sliding, which was not shown on Ashby and Verrall's original map, has been added in orange. The activation area of SIA-induced GB sliding has been added in yellow. Deformation mechanism maps usually depict the primary deformation mechanism, although other mechanisms may still be present. The aim of this map is simply to identify areas where these mechanisms may contribute; it does not claim that they are dominant.

5. Conclusions

Based on *in situ* deformation experiments on sub-micron olivine bicrystals at RT, we show that GBs are weak zones where SIA preferentially occurs. Molecular dynamics modelling confirms the TEM observation that no other plasticity mechanism is activated, either in the crystals or in the GB. It shows that the cumulative plastic strain is proportional to the thickness of the amorphous layer that localizes the shear. SIA-induced GB sliding is therefore a distinct deformation mechanism competing with fracture at low temperatures. The difference in behavior between Mg-rich and Fe-rich olivine shows that chemistry is an important factor controlling this behavior. The very fine scale heterogeneity of the information leads us to postulate that the structure of the GB is likely to be equally important.

These observations open up prospects beyond olivine for controlling the properties of hard materials at low temperatures. While GBs are generally considered to be hardening and embrittling elements, we show that controlling their structures (possibly through their chemistry) can promote some ductility in a domain where no other mechanism is active.

Data availability

Data will be made available on request.

CRediT authorship contribution statement

Ihtasham Ul Haq: Writing – review & editing, Visualization, Investigation, Formal analysis. **Patrick Cordier:** Writing – review & editing, Validation, Supervision, Project administration, Methodology, Funding acquisition, Conceptualization. **Jean Furstoss:** Software, Investigation, Formal analysis. **Karine Gouriet:** Software, Investigation, Formal analysis. **Ankush Kashiwar:** Software, Investigation, Formal analysis. **Paul Baral:** Software, Investigation, Formal analysis. **Andrey Orekhov:** Software, Formal analysis. **Nicolas Gauquelin:** Investigation, Formal analysis. **Sanae Koizumi:** Resources. **Caroline Bollinger:** Resources. **Laurent Delannay:** Formal analysis. **Philippe Carrez:** Writing – review & editing, Supervision. **Thomas Pardoen:** Writing – review & editing. **Dominique Schryvers:** Writing – review & editing, Validation, Supervision. **Hosni Idrissi:** Writing – original draft, Validation, Supervision, Project administration, Methodology, Conceptualization.

Declaration of competing interest

The authors declare that they have no known competing financial interests or personal relationships that could have appeared to influence the work reported in this paper.

Acknowledgements

This project has received funding from the European Research Council (ERC) under the European Union's Horizon 2020 research and innovation programme under grant agreement No 787198 – TimeMan. H. Idrissi is mandated by the Belgian National Fund for Scientific Research (FSR- FNRS). This work was supported by the FNRS under Grant PDR –T011322F and the Programme 'Actions de Recherche concertées (ARC)' of the Fédération Wallonie-Bruxelles (re: project 'NanoGG' ref. nbr. 23/27–132).

Supplementary materials

Supplementary material associated with this article can be found, in the online version, at doi:10.1016/j.actamat.2025.121697.

References

[1] X. Fang, A. Nakamura, J. Rödel, Deform to perform: dislocation-tuned properties of ceramics, Am. Ceram. Soc. Bull. 102 (2023) 24–29. https://ceramics.org/wp-content/bulletin/2023/pdf/JuneJuly-2023.pdf#page=26.

[2] M. Pec, H. Stünitz, R. Heilbronner, M. Drury, Semi-brittle flow of granitoid fault rocks in experiments, J. Geophys. Res. Solid Earth 121 (2016) 1677–1705, https://doi.org/10.1002/2015JB012513.

[3] H. Idrissi, A. Béché, N. Gauquelin, I. Ul-Haq, C. Bollinger, S. Demouchy, J. Verbeeck, T. Pardoen, D. Schryvers, P. Cordier, On the formation mechanisms of intragranular shear bands in olivine by stress-induced amorphization, Acta Mater 239 (2022) 118247, https://doi.org/10.1016/j.actamat.2022.118247.

[4] B.Y. Li, A.C. Li, S. Zhao, M.A. Meyers, Amorphization by mechanical deformation, Mater. Sci. Eng. R: Report. 149 (2022) 100673, https://doi.org/10.1016/j.mser.2022.100673.

[5] H. Luo, H. Sheng, H. Zhang, F. Wang, J. Fan, J. Du, J.Ping Liu, I. Szlufarska, Plasticity without dislocations in a polycrystalline intermetallic, Nat. Comm. 10 (2019) 3587, https://doi.org/10.1038/s41467-019-11505-1.

[6] K. Kranjc, A.S. Thind, A.Y. Borisevich, R. Mishra, K.M. Flores, P. Skemer, Amorphization and plasticity of olivine during low-temperature micropillar deformation experiments, J. Geophys. Res. Solid Earth. 125 (2020), https://doi.org/10.1029/2019JB019242 e2019JB019242.

[7] V. Samae, P. Cordier, S. Demouchy, C. Bollinger, J. Gasc, S. Koizumi, A. Mussi, D. Schryvers, H. Idrissi. Stress-induced amorphization triggers deformation in the lithospheric mantle. Nature 591, 82–86. https://doi.org/10.1038/s41586-021-03238-3.

[8] J. Gasc, S. Demouchy, F. Barou, S. Koizumi, P. Cordier, Creep mechanisms in the lithospheric mantle inferred from deformation of iron-free forsterite aggregates at 900–1200 °C, Tectonophysics 761 (2019) 16–30, https://doi.org/10.1016/j.tecto.2019.04.009.

[9] H. Idrissi, C. Bollinger, F. Boioli, D. Schryvers, P. Cordier, Low-temperature plasticity of olivine revisited with *in situ* TEM nanomechanical testing, Sci. Adv. 2 (2016) e1501671, https://doi.org/10.1016/j.actamat.2016.01.019.

[10] H. Idrissi, V. Samaee, G. Lumbeeck, T. van der Werf, T. Pardoen, D. Schryvers, P. Cordier, *In situ* quantitative tensile testing of antigorite in a transmission electron microscope, J. Geophys. Res.: Solid Earth. 125 (3) (2020), https://doi.org/10.1029/2019JB018383 e2019JB018383.

[11] Y. Xiao, V. Maier-Kiener, J. Michler, R. Spolenak, J.M. Wheeler, Deformation behavior of aluminum pillars produced by Xe and Ga focused ion beams: insights from strain rate jump tests, Mater. Des. 181 (2019) 107914, https://doi.org/10.1016/j.matdes.2019.107914.

[12] Y. Xiao, J. Wehrs, H. Ma, T. Al-Samman, S. Korte-Kerzel, M. Goken, J. Michler, R. Spolenak, J.M. Wheeler, Investigation of the deformation behavior of aluminum micropillars produced by focused ion beam machining using Ga and Xe ions, Scr. Mater. 127 (2017) 191e194, https://doi.org/10.1016/j.scriptamat.2016.08.028.

[13] M. Naderi, M. Peterlechner, E. Schafler, S.V. Divinski, G. Wilde, Kinetic, volumetric and structural effects induced by liquid Ga penetration into ultrafine grained Al, Acta Mater 99 (2015) 196–205, https://doi.org/10.1016/j.actamat.2021.117145.

[14] S. Zhao, Z. Li, Ch. Zhu, W. Yang, Z. Zhang, D.E.J. Armstrong, P.S. Grant, R. O. Ritchie, M.A. Meyers, Amorphization in extreme deformation of the CrMnFeCoNi high-entropy alloy, Sci. Adv. 7 (2021) 1–7, https://doi.org/10.1126/sciadv.abb3108.

[15] S. Zhao, R. Flanagan, E.N. Hahn, B. Kad, B.A. Remington, C.E. Wehrenberg, R. Cauble, K. More, M.A. Meyers, Shock-induced amorphization in silicon carbide acta mat., 158 (2018), 206–213. https://doi.org/10.1016/j.actamat.2018.07.047.

[16] M.W. Chen, K.J.Hemker McCauley, Shock-induced localized amorphization in boron carbide, Science 299 (2003) 1563–1566, https://doi.org/10.1126/science.1080819.

[17] I.A. Ovid'ko, Nanoscale amorphization as a special deformation mode in nanowires, Scripta Mat 66 (2012) 402–405, https://doi.org/10.1016/j.scriptamat.2011.12.001.

[18] X. Wu, N. Tao, Y. Hong, J. Lu, K. Lu, K, localized solid-state amorphization at grain boundaries in a nanocrystalline Al solid solution subjected to surface mechanical attrition, J. Phys. D Appl. Phys. 38 (2005) 4140–4143. http://doi.org/10.1088/0022-3727/38/22/019.

[19] C.C. Koch, J.D. Whittenberger, Mechanical milling/alloying of intermetallics, Intermetallics 5 (1996) 339–355, https://doi.org/10.1016/0966-9795(96)00001-5.

[20] R. Jeanloz, T.J. Ahrens, J.S. Lally, G.L. Nord, J.M. Christie, A.H. Heuer, Shock-produced olivine glass: first observation, Science 197 (4302) (1977) 457–459. http://doi.org/10.1126/science.197.4302.457.

[21] J. Blaber, B. Adair, A. Antoniou, Ncorr: open-source 2D digital image correlation matlab software, Exp. Mech. 55 (2015) 1105–1122, https://doi.org/10.1007/s11340-015-0009-1.

[22] S.J. Plimpton, Fast parallel algorithms for short-range molecular dynamics, J. Comput. Phys. 117 (1995) 1–19, https://doi.org/10.1006/jcph.1995.1039.

[23] A. Pedone, G. Malavasi, M.C. Menziani, A.N. Cormack, U. Segre, A new self-consistent empirical interatomic potential model for oxides, silicates, and silicas-based glasses, J. Phys. Chem. B. 110 (2006) 11780–11795, https://doi.org/10.1021/jp0611018.

[24] J.W. Eastwood, R.W. Hockney, D.N. Lawrence, P3M3DP—The three-dimensional periodic particle-particle/particle-mesh program, Comput. Phys. Comm. 19 (1980) 215–261, https://doi.org/10.1016/0010-4655(80)90052-1.

[25] P. Hirel, J. Furstoss, P. Carrez, A critical assessment of interatomic potentials for modelling lattice defects in forsterite Mg_2SiO_4 from 0 to 12 GPa, Phys. Chem. Miner. 48 (2021) 46, https://doi.org/10.1007/s00269-021-01170-6.

[26] J. Furstoss, P. Hirel, P. Carrez, P. Cordier, Complexions and stoichiometry of the 60.8°//[100](011) symmetrical tilt grain boundary in Mg_2SiO_4 forsterite: a combined empirical potential and first-principles study, Am. Miner. 107 (11) (2022) 2034–2043, https://doi.org/10.2138/am-2022-8420.

[27] J. Furstoss, P. Hirel, P. Carrez, K. Gouriet, V. Meko-Fotso, P. Cordier, Structures and energies of twist grain boundaries in Mg_2SiO_4 forsterite, Comput. Mater. Sci. 233 (2024) 112768, https://doi.org/10.1016/j.commatsci.2023.112768.

[28] G. Kresse, J. Furthmüller, Efficient iterative schemes for ab initio total-energy calculations using a plane-wave basis set, Phys. Rev. B. 54 (1996) 11169–11186, https://doi.org/10.1103/PhysRevB.54.11169.

[29] J.P. Perdew, Y. Wang, Accurate and simple analytic representation of the electron-gas correlation-energy, Phys. Rev. B. 98 (2018) 079904, https://doi.org/10.1103/PhysRevB.45.13244.

[30] Y. Wang, J.P. Perdew, Correlation hole of the spin-polarized electron gas, with exact small-wave-vector and high-density scaling, Phys. Rev. B 44 (1991) 13298, https://doi.org/10.1103/PhysRevB.44.13298.

[31] S. Stackhouse, L. Stixrude, B.B. Karki, Determination of the high-pressure properties of fayalite from first-principles calculations, Earth Planet. Sci. Lett. 289 (2010) 449–456, https://doi.org/10.1016/j.epsl.2009.11.033.

[32] S.L. Dudarev, G.A. Botton, S.Y. Savrasov, C.J. Humphreys, A.P. Sutton, Electron-energy-loss spectra and the structural stability of nickel oxide: an LSDAU study, Phys. Rev. B. 57 (1998) 1505, https://doi.org/10.1103/PhysRevB.57.1505.

[33] E.R. Hernández, J. Brodholt, D. Alfè, Structural, vibrational and thermodynamic properties of Mg_2SiO_4 and $MgSiO_3$ minerals from first-principles simulations, Phys. Earth Planet. Int. 240 (2015) 1–24, https://doi.org/10.1016/j.pepi.2014.10.007.

[34] P. Lazar, R. Podloucky, Cleavage fracture of a crystal: density functional theory calculations based on a model which includes structural relaxations, Phys. Rev. B. 78 (2008) 104114, https://doi.org/10.1103/PhysRevB.78.104114.

[35] J.H. Rose, J.R. Smith, J. Ferrante, Universal features of bonding in metals, Phys. Rev. B (1983) 1835, https://doi.org/10.1103/PhysRevB.28.1835.

[36] O. Adjaoud, K. Marquardt, S. Jahn, Atomic structures and energies of grain boundaries in Mg_2SiO_4 forsterite from atomistic modeling, Phys. Chem. Mineral. 39 (2012) 749–760, https://doi.org/10.1007/s00269-012-0529-5.

[37] A. Orekhov, G. Kermouche, A. Gomez-Perez, P. Baral, R. Dohmen, M. Coulombier, J. Verbeeck, T. Pardoen, D. Schryvers, J. Lin, P. Cordier, H. Idrissi, Room temperature electron beam sensitive viscoplastic response of ultra-ductile amorphous olivine films, Acta. Mat 282 (2024) 120479, https://doi.org/10.1016/j.actamat.2024.120479.
[38] V. Delbecq, P. Carrez, P. Cordier, Rheological properties of Mg2SiO4 glass: a molecular dynamics study, J. Non-Cryst. Solid. 619 (2023) 122572, https://doi.org/10.1016/j.jnoncrysol.2023.122572.
[39] S. Demouchy, A. Tommasi, T. Boffa Ballaran, P. Cordier, Low strength of Earth's uppermost mantle inferred from tri-axial deformation experiments on dry olivine crystals, Phys. Earth Planet. Int. 220 (2013) 37–49, https://doi.org/10.1016/j.pepi.2013.04.008.
[40] P.R. Cantwell, M. Tang, S.J. Dillon, J. Luo, G.S. Rohrer, M.P. Harmer, Grain boundary complexions, Acta. Mat 62 (2014) 1–48, https://doi.org/10.1016/j.actamat.2013.07.037.
[41] S.J. Dillon, M.P. Harmer, J. Luo, J. Grain boundary complexion in ceramic and metals an overview, JOM 61 (2009) 38–44, https://doi.org/10.1007/s11837-009-0179-3.
[42] T. Frolov, D.L. Olmsted, M. Asta, Y. Mishin, Structural phase transformations in metallic grain boundaries, Nat. Commun. 4 (2013) 1899, https://doi.org/10.1038/ncomms2919.
[43] Y.H. Zhao, M.E. Zimmerman, D.L. Kohlstedt, Effect of iron content on the creep behavior of olivine: 1. Anhydrous conditions, Earth Planet. Sci. Lett. 287 (2009) 229–240, https://doi.org/10.1016/j.epsl.2009.08.006.
[44] X. Hu, N. Liu, V. Jambur, S. Attarian, R. Su, H. Zhang, J. Xi, H. Luo, J. Perepezko, I. Szlufarska, Amorphous shear bands in crystalline materials as drivers of plasticity, Nature Mater 22 (2023) 1071–1077, https://doi.org/10.1038/s41563-023-01597-y.
[45] M.F. Ashby, R.A. Verrall, Micromechanisms of flow and fracture, and their relevance to the rheology of the upper mantle, Philos. Trans. R. Soc. A-Math Phys. Eng. Sci. 288 (1977) 59–95, https://doi.org/10.1098/rsta.1978.0006.
[46] B.-N. Kim, K. Hiraga, Contribution of grain boundary sliding in diffusional creep, Scripta Mater 42 (2000) 451–456, https://doi.org/10.1016/S1359-6462(99)00369-3.
[47] G. Maruyama, T. Hiraga, Grain- to multiple-grain-scale deformation processes during diffusion creep of forsterite + diopside aggregate: 1. Direct observations, J. Geophys. Res. Solid Earth 122 (2017) 5890–5915, https://doi.org/10.1002/2017JB014254.
[48] R. Raj, M.F. Ashby, On grain boundary sliding and diffusional creep, Metall. Trans. 2 (1971) 1113–1127, https://doi.org/10.1007/BF02664244.
[49] G. Hirth, D.L. Kohlstedt, Experimental constraints on the dynamics of the partially molten upper mantle: 2. Deformation in the dislocation creep regime, J. Geophys. Res. 100 (1995) 15441–15449, https://doi.org/10.1029/95JB01292.
[50] J.M. Warren, G. Hirth, Grain size sensitive deformation mechanisms in naturally deformed peridotites, Earth Planet. Sci. Lett. 248 (2006) 438–450, https://doi.org/10.1016/j.epsl.2006.06.006.
[51] P. Cordier, S. Demouchy, B. Beausir, V. Taupin, F. Barou, C. Fressengeas, Disclinations provide the missing mechanism for deforming olivine-rich rocks in the mantle, Nature 507 (2014) 51–56, https://doi.org/10.1038/nature13043.
[52] J.P. Hirth, G. Hirth, J. Wang, Disclinations and disconnections in minerals and metals, PNAS 117 (2020) 196–204, https://doi.org/10.1073/pnas.1915140117.
[53] I. Jackson, U.H. Faul, J.D. Fitz Gerald, S.J.S. Morris, Contrasting viscoelastic behavior of melt-free and melt-bearing olivine: implications for the nature of grain-boundary sliding, Mater. Sci. Eng. A. 442 (2006) 170–174, https://doi.org/10.1016/j.msea.2006.01.136.